Planar microcavity-integrated hot-electron photodetector

Cheng Zhang,[a,b] Kai Wu,[a,b] Yaohui Zhan,[a,b] Vincenzo Giannini[c] and Xiaofeng Li*[a,b]

Hot-electron photodetectors are attracting increasing interest due to their capability in below-bandgap photodetection without employing classic semiconductor junctions. Despite the high absorption in metallic nanostructures *via* plasmonic resonance, the fabrication of such devices is challenging and costly due to the use of high-dimensional sub-wavelength nanostructures. In this study, we propose a planar microcavity-integrated hot-electron photodetector (MC-HE PD), in which the TCO/semiconductor/metal (TCO: transparent conductive oxide) structure is sandwiched between two asymmetrically distributed Bragg reflectors (DBRs) and a lossless buffer layer. Finite-element simulations demonstrate that the resonant wavelength and the absorption efficiency of the device can be manipulated conveniently by tailoring the buffer layer thickness and the number of top DBR pairs. By benefitting from the largely increased electric field at the resonance frequency, the absorption in the metal can reach 92%, which is a 21-fold enhancement compared to the reference without a microcavity. Analytical probability-based electrical calculations further show that the unbiased responsivity can be up to 239 nA mW^{-1}, which is more than an order of magnitude larger than that of the reference. Furthermore, the MC-HE PD not only exhibits a superior photoelectron conversion ability compared to the approach with corrugated metal, but also achieves the ability to tune the near infrared multiband by employing a thicker buffer layer.

1. Introduction

Hot-electron photodetectors have recently attracted significant attention due to the advantages of detecting photon energy well below the semiconductor band edge, operating in room temperature, and providing a highly controllable detection wavelength on resonance.[1–15] Besides photodetection, hot electrons can be directly harnessed for a broad range of applications, *e.g.*, photovoltaics,[16,17] photocatalysis,[18,19] and surface imaging.[20,21] Indeed, the hot electrons arising from surface plasmonic decay can be collectively harnessed to generate a photocurrent, provided that the incident photon energy is high enough to overcome the Schottky barrier.[2] In 2011, Knight *et al.* proposed the concept of using an active plasmonic nanoantenna that combines light harvesting and electrical conversion together to detect long-wavelength light well below the band edge of the semiconductor.[1] Among the various designs, the metallic nanostructures including nanorods,[1,3] nanowires,[4] gratings,[5–7] and waveguides[8] have been proven to be efficient. For example, a distinct enhancement in photo-responsivity was achieved in the deep-trench/thin-metal active antennas largely due to the high optical absorption as a result of the cavity effect;[6] an ultrathin metamaterial perfect absorber can result in near-unity optical absorption in the hot-electron photodetector with a very high photoresponsivity.[7] In addition, an alternative approach is to employ the metal–insulator–metal (M–I–M) structure, which reshapes one of the metallic contacts into a plasmonic antenna so that the incident electromagnetic energy can be trapped efficiently for photocurrent generation.[9] Our recent study shows as well that a multi-layered conformal grating can improve the responsivity to be 3 times that based on a conventional grating system due to the strong and highly asymmetrical optical absorption between the top and bottom metal layers.[10]

However, it is generally challenging and costly to fabricate these metallic nanostructures on a sub-wavelength scale.[22] To develop low-cost photodetection technology, a cheap fabrication process is desired, which suggests the use of conventional planar systems.[23,24] However, a planar system without a

[a]College of Physics, Optoelectronics and Energy & Collaborative Innovation Center of Suzhou Nano Science and Technology, Soochow University, Suzhou 215006, China. E-mail: xfli@suda.edu.cn
*[b]Key Lab of Advanced Optical Manufacturing Technologies of Jiangsu Province & Key Lab of Modern Optical Technologies of Education Ministry of China, Soochow University, Suzhou 215006, China*
[c]Blackett Laboratory, Imperial College London, Prince Consort Road, London SW7 2BZ, UK

delicate design always shows a weak light-trapping capability. It is therefore highly desirable to investigate the design of a planar photodetection system with strong optical absorption and a high photoconversion efficiency. Inspired by the fact that a strongly enhanced optical field can be achieved in an asymmetric Fabry–Perot (FP) cavity,[25–28] we report a planar microcavity-integrated hot-electron photodetector (MC-HE PD), where the core electrical section, i.e., TCO/semiconductor/metal (TCO/S/M, TCO: transparent conductive oxide), is sandwiched between the partially transmitting top and highly reflective bottom distributed Bragg reflectors (DBRs). A buffer layer is employed to control the FP resonance towards the target wavelength. It is noted that the semiconductor used here is intrinsic, which makes the device substantially different from the conventional metal/semiconductor (M/S) systems based on Schottky junctions and it could be operated under the same working principles as those reported in ref. 9–12. The barrier height (φ_B) is expected to be decreased through the replacement of the insulator with a wide-bandgap semiconductor with a larger electron affinity χ ($\varphi_B = W - \chi$, W: the work function), which extends the detectable wavelength range, facilitates electron transport through the barrier, and thus improves the photoresponsivity. Electromagnetic simulation shows that more than 92% of the incident light can be preferentially absorbed by the metal layer under resonance, showing a 21-fold absorption enhancement compared to that of the reference without a microcavity. Such strongly asymmetric optical absorption between the two electrodes (TCO and metal) leads to a high and unidirectional photocurrent. Analytical probability-based electrical calculations further demonstrate that the photoresponsivity can be up to 239 nA mW^{-1} at zero bias voltage, which is more than an order of magnitude larger than that based on the planar system without a microcavity. Moreover, the planar hot-electron photodetection system exhibits strong tunability for the operating wavelength, a superior photoelectron conversion ability compared to the other approaches with corrugated metal layers, and multiband selectivity in the near-infrared band by employing a thicker buffer layer. Therefore, it is expected to be a promising low-cost, highly sensitive candidate for multiband photodetection applications based on hot-electron injection.

2. Microcavity-integrated hot-electron photodetectors (MC-HE PDs)

Based on the understanding of microcavity resonance,[25–28] we combine strong field confinement by the microcavity with hot-electron photodetection to realize a planar MC-HE PD with high photoresponsivity. The schematic diagram of the proposed MC-HE PD is shown in Fig. 1(a), which shows that it is composed of the silica substrate, bottom DBR, buffer layer, TCO/S/M stack, and top DBR. When targeting at a wavelength of 850 nm, the top (bottom) DBR consists of 2 (10) pairs of Si$_3$N$_4$/SiO$_2$ (TiO$_2$/SiO$_2$) and each layer has an optical thickness
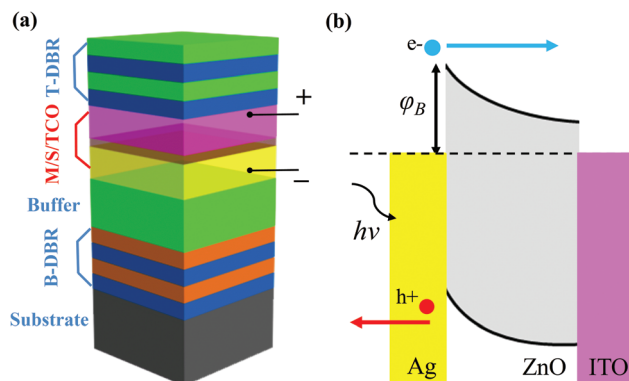
Fig. 1 (a) Schematic diagram of the planar microcavity-integrated hot-electron photodetector. (b) Energy band diagram for the TCO/S/M structure with a barrier height of φ_B. Hot electrons are generated in either contact and collected by the opposite electrode.

of a quarter of the central wavelength. The thicknesses of the TCO (ITO), semiconductor (ZnO), metal (Ag), and buffer (Si$_3$N$_4$) layers are 20, 5, 20, and 193 nm, respectively. The potential barrier for the ZnO/Ag interface is ~0.6 eV.[29,30] A bias potential across the device is simulated and the light is incident normally to the device. Fig. 1(b) shows the energy band diagram of the TCO/S/M device with a barrier height of φ_B.[31,32] The performance of the MC-HE PD can be determined by considering the following consecutive steps:[9–11,24] (1) the generation of energetic hot electrons upon the absorption of photon energy, (2) the diffusion to the interface without losing energy in an inelastic collision, (3) the injection into the semiconductor, (4) the propagation across the semiconductor without inelastic collisions, and (5) the collection by the opposite electrode. In the end, the total photocurrent is the difference in the counter-propagating electrons flowing from both electrodes. This reveals that asymmetrical optical absorption and band alignment are essential to obtain high photoresponsivity.[10,33]

Based on the optical constants from Palik's work,[34] the optical simulations are performed by solving Maxwell's equations via the finite-element method.[35] Besides, rigorous coupled-wave analysis (RCWA) is employed to study the optical dispersion characteristics due to its fast response.[36] The absorption efficiency (P_{abs}) is defined as:[37]

$$P_{abs}(\lambda) = \frac{\iiint_V Q_{rh}(x,y,z,\lambda)\,dV}{P_{in}} \quad (1)$$

where P_{in} is the incident power and Q_{rh} is the absorbed power volume–density inside the device with volume V. Q_{rh} is calculated under Poynting's theorem:
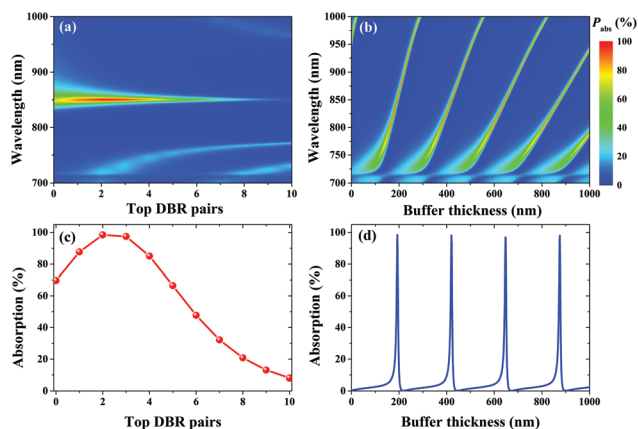
$$Q_{rh}(x,y,z,\lambda) = \frac{1}{2}\varepsilon_i\omega|E(x,y,z,\lambda)|^2 \quad (2)$$

where ω is the angular frequency, ε_i is the imaginary part of the material permittivity, and $E(x, y, z)$ is the electric field at position (x, y, z).

3. Absorption and photoconversion of the MC-HE PD

In the MC-HE PD, the incident light is mostly absorbed by the Ag and ITO layers at the target wavelength. To explore the resonance tunability of the device, we focus on how to control the overall absorption of the device in terms of adjusting the number of top DBR pairs and the thickness of the buffer layer. The corresponding results are displayed in Fig. 2(a) and (b), respectively. Fig. 2(a) shows that: (1) the planar microcavity can absorb almost the entire incident energy under resonance; (2) the number of top DBR pairs has a weak impact on the resonant wavelength, but greatly modifies the absorption efficiency. This is because a highly-reflective top DBR prevents the light incidence from penetrating into the microcavity and leads to a low absorption;[38] however, a lowly-reflective top DBR cannot form a good microcavity to well confine the light. Therefore, the design of the top DBR is a crucial factor to obtain the highest optical performance. On the other hand, Fig. 2(b) indicates that the buffer thickness is another key parameter which is used to tune the resonance.[25] There is a very wide tunable range for the resonance, i.e., 700 nm–1000 nm, by varying the buffer layer thickness. However, as shown in Fig. 2(b), the resonant wavelength does not show a linear dependence on the buffer thickness due to the cavity and material dispersions.
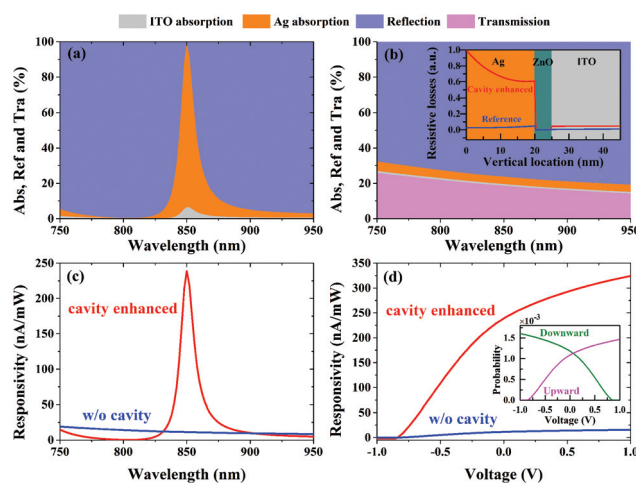
At the detection wavelength of 850 nm, the absorption efficiency versus the number of top DBR pairs and the buffer layer thickness is illustrated in Fig. 2(c) and (d), respectively. It is clear that there is an absorption peak of ~98.5% when 2 pairs of top DBR layers are used; on increasing the layer number, the absorption drops to a very low value (<10%). On the contrary, the absorption efficiency at resonance exhibits a typical periodic dependence on the thickness of the buffer layer, i.e., a period of $\lambda/2n \sim 227$ nm ($n = 1.87$ for the buffer index at a wavelength of 850 nm).

The detailed optical responses of the MC-HE PD are illustrated in Fig. 3(a). It is shown that at the resonance frequency most of the light is absorbed by the Ag layer ($P_{Ag} = 92.4\%$) and the parasitic absorption in the ITO layer is tiny ($P_{ITO} = 6.1\%$).[23] Comparably, in this case, the reflection loss of the device is negligible ($R = 1.2\%$). However, for the off-resonance cases, $R \sim 100\%$ is observed as a result of the highly reflective nature of DBRs (without the microcavity coupling),[26] leading to an extremely low absorption. For reference, the spectral responses of the planar TCO/S/M stacks without a microcavity are plotted in Fig. 3(b). Due to the thin thicknesses of ITO and Ag, most of the light is reflected at the surface or transmitted through the device, leaving a very small portion of the incident energy for photocurrent generation. Quantified examination of the absorption by the Ag layer indicates that a 21-fold absorption enhancement is achieved in the microcavity-integrated device (92.4%) compared to the reference (4.18%).

Besides the absorption efficiency, the spatial distribution of the hot electrons also plays an important role in determining the photoconversion procedure.[39] This is because the generated hot electrons encounter different kinds of losses during the carrier transport process and these losses are always strongly space-dependent. The spatial distributions of the resistive losses (absorbed power volume–density) in the two devices are illustrated in the inset of Fig. 3(b). Due to the preferential absorption by the Ag layer in the MC-HE PD, the number of hot electrons generated in the Ag layer is greatly larger than that in the ITO layer, causing a strong hot-electron flow from Ag to ITO. Although the power absorption is decreased gradually towards the M/S interface, the probability for the hot electrons to arrive at the M/S interface is relatively large due to the thin thickness of Ag (20 nm).[23] In contrast, for

Fig. 2 The contour maps of the total absorption as a function of the incident wavelength and (a) the top DBR pair number and (b) the buffer layer thickness. Total absorption versus (c) the number of top DBR pairs and (d) the buffer layer thickness at the targeted wavelength of 850 nm.

Fig. 3 The detailed optical responses in (a) the MC-HE PD and (b) the reference device without a microcavity. The spatial distributions of the resistive losses (absorbed power volume–density) are shown in the inset of (b). The responsivities versus (c) the wavelength and (d) the electrical voltage (at $\lambda = 850$ nm) in the MC-HE PD and the reference without a microcavity. The probabilities of the upward and downward transmissions of the hot electrons as a function of the applied bias voltage are shown in the inset of (d).

the reference device, the number of hot electrons generated in both electrodes is equivalently small, giving rise to a low photocurrent.

With the spatial distributions of the hot electrons, the electrical response of the device can be determined by addressing the transport process carefully. Based on the assumption of an isotropic initial momentum distribution of the hot electrons,[2,9–11] only half of them will diffuse towards the M/S interface. The probability that a hot electron reaches the semiconductor without losing energy in an inelastic collision is quantified by taking account of the mean free path (MFP) of energetic electrons in solids:[24]

$$P_1(z) = \frac{1}{2\pi} \int_0^\pi \exp\left[-\frac{d(z)}{\lambda_e|\cos(\theta)|}\right] d\theta \quad (3)$$

where d is the shortest distance from the initial position of the hot electrons to the M/S interface, λ_e is the MFP of the hot electrons in Ag/ITO,[40,41] and θ is the electron diffusion angle. The flux of the electrons reaching the interface is expressed as:

$$N = N_{ph} \int \frac{Q_{rh(Z)}}{P_{in}} P_1(z) dz \quad (4)$$

where N_{ph} is the incident photon flux. The internal quantum efficiency (η_i) is defined as the probability that the electrons accumulated at the boundary will successfully tunnel across the interface and finally be collected by the opposite electrode. Based on the assumption of a constant electron density of states (EDOS),[9] η_i is calculated using the probability of the electrons to climb across the barrier (P_2), propagate through the semiconductor (P_3), and transmit into the other electrode (P_4):

$$\eta_i = \frac{1}{E_{ph}} \int_{\phi_B}^{E_{ph}} P_2 P_3 P_4(E) dE \quad (5)$$

where E_{ph} is the incident photon energy. The general formulas for the calculations of P_2, P_3, and P_4 can be found in the ESI of ref. 9. Therefore, the total photocurrent density can be written as:

$$\begin{aligned} J_{Net} &= \left| J_{ITO\to Ag} - J_{Ag\to ITO} \right| \\ &= e\left| N_{Ag\to ITO} \times \eta_{i,Ag\to ITO} - N_{ITO\to Ag} \times \eta_{i,ITO\to Ag} \right| \end{aligned} \quad (6)$$

where $N_{Ag\to ITO}$ ($N_{ITO\to Ag}$) is the flux of the hot electrons reaching the M/S (TCO/S) interface, and $\eta_{i,Ag\to ITO}$ ($\eta_{i,ITO\to Ag}$) is the internal quantum efficiency of the hot electrons from Ag to TCO (TCO to Ag). It should be noted that the photocurrent direction is the reverse of the electron flowing direction due to the negative charge of the electron, i.e., $J_{ITO\to Ag}$ ($J_{Ag\to ITO}$) corresponds to $N_{Ag\to ITO}$ & $\eta_{i,Ag\to ITO}$ ($N_{ITO\to Ag}$ & $\eta_{i,ITO\to Ag}$).

Following the procedures described above, the wavelength-dependent photoresponsivities of the MC-HE PD and the planar reference without a microcavity are shown in Fig. 3(c). It is apparent that the absorption and responsivity spectra are highly similar, indicating that prominent absorption is a requisite for a good electrical performance. A strong photoresponse peak of ~239 nA mW^{-1} is predicted at the resonant wavelength

of 850 nm in the MC-HE PD, which is more than an order of magnitude larger than that of the reference (11 nA mW^{-1}). A spectral width of ~13 nm (full width at half maximum, FWHM) is observed for the resonance, which is sharp enough for high-sensitivity and narrow-band photodetection/sensing applications.[10] Nevertheless, the spectral response of the reference device is almost flat, showing that no cavity resonance has been excited.

Fig. 3(d) plots the responsivities of the hot-electron photodetectors with and without a microcavity as a function of the electric voltage. When the positive contact is connected to TCO and the negative to the silver layer, it is called forward electric bias. The results indicate that forward (reverse) bias greatly enhances (degrades) the responsivity of the performances for both devices. Taking the MC-HE PD as the example, the responsivity is 307 nA mW^{-1} at $V = 0.8$ V, showing an increment of 68 nA mW^{-1} compared to that at $V = 0$ V; while if V is decreased to -0.86 V, no photocurrent can be obtained with a responsivity of close to 0 nA mW^{-1}. Such a clear onset in the photocurrent is closely related to the highest point in the barrier that allows significantly more hot electrons to travel across the barrier, which is increased with higher reverse electric bias. The total transmission probabilities of the hot electrons towards the top (upward, Ag → ITO) and bottom (downward, ITO → Ag) contacts as a function of the electric bias are plotted in the inset of Fig. 3(d). It is clear that applying a forward bias contributes to a higher upward transmission probability since the kinetic energy of the electrons in the semiconductor is promoted and thus so is the transmission probability of P_4.[23] As most of the hot electrons are generated in the Ag layer in the bottom, this can give rise to a net photocurrent from the top to bottom contacts as long as there is a high upward transmission probability even when the reverse bias is applied.

We now investigate the influence of the Ag thickness on the optical and electrical responses in the MC-HE PD. It should be noted that, for each Ag thickness a complete screening of the number of top DBR pairs and the buffer layer thickness has been carried out using RCWA to identify the optically "optimal" design, which gives rise to a maximal absorption in the TCO/S/M stack. The calculated optical responses (absorption, reflection, and transmission) against the Ag thickness are shown in Fig. 4. It is found that almost all of the incoming light can be absorbed in the device even with an ultrathin Ag layer (e.g., 5 nm), if we properly control the number of top DBR pairs and the buffer layer thickness.[26] The physical reason for this lies in the microcavity resonance providing very good field confinement of the incident light, forming a strong coupling with the TCO/S/M layers and resulting in high absorption.[38,42] It is further observed that with increasing Ag thickness, the absorption in ITO is decreased gradually, which results in a steadily enhanced net absorption, i.e., P_{Ag}–P_{ITO} (see the magenta curve). However, the electrical simulation indicates that higher asymmetric absorption does not certainly lead to a high responsivity (see the blue curve, which however shows a peak at the Ag thickness of 10 nm). This is rational since a
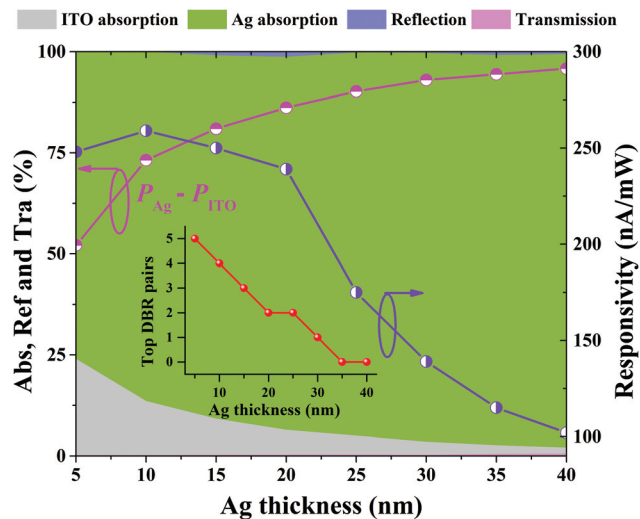
Fig. 4 The detailed optical responses in the optically optimized configurations for each metal thickness at λ = 850 nm. The corresponding net optical absorption and the device responsivity *versus* Ag thickness are shown as well. The inset shows the designed number of top DBR pairs at each metal thickness.

metal film with a thickness beyond the MFP of the electrons could dramatically degrade the internal electron transportation efficiency.[9] We also find that a lower number of top DBR pairs is required to achieve an optimal system absorption, if a thicker Ag layer is used (see the inset of Fig. 4). This is because a thicker bottom Ag film provides stronger optical reflection, which allows the top DBR to have relatively lower reflection (*i.e.*, fewer DBR pairs).

Furthermore, we would like to demonstrate that the concept can be extended to the infrared band with an energy far below the band gap of the semiconductor. Since the net photocurrent is mainly determined by the upward transmission of the hot electrons from Ag to ITO, the absorption spectra for the 10 nm Ag layer of the designed MC-HE PD at the operating wavelengths of 1250, 1350, 1450, 1550, and 1650 nm are plotted in Fig. 5(a). It is clear that ~90% of the light is absorbed by Ag for all of the considered wavelengths, which is close to the value of the system operating at the wave-

length of 850 nm. The corresponding responsivities of the unbiased MC-HE PD are shown in Fig. 5(b) where the results of the conventional grating systems are shown for comparison (see the inset).[12] Notably, although the absorption efficiencies at the various operating wavelengths are similar, the responsivities towards the longer wavelengths are gradually decreased since the energy-dependent internal transmission probability is decreased.[2,9] Moreover, in microcavity design the planar system exhibits obvious advantages for hot-electron photoconversion compared to the grating-based counterparts, *e.g.*, at λ = 1550 nm, the responsivity of the MC-HE PD is 17.3 nA mW^{-1}, which is ~2.5 times that of the grating system (*i.e.*, 7 nA mW^{-1}).

Next, we would like to indicate that multiband photodetection can be readily realized in the proposed MC-HE PD by tuning the cavity resonances. This is because in the one-dimensional photonic crystal a thicker defect layer can lead to more high-order defect modes propagating within the forbidden band,[43–45] enabling multiband hot-electron photodetection. The contour maps of the reflection and total absorption as a function of the incident wavelength & buffer layer thickness are shown in Fig. 6(a) and (b), respectively. Since the buffer layer considered is relatively thick, multiple resonant bands can be clearly seen from these two figures. Choosing a buffer thickness of 2000 nm, the reflection and total absorption spectra of the MC-HE PD are displayed in Fig. 6(c), where the dashed curve plots the reflection spectrum of the bottom DBR. Three sharp resonances are manifested by the distinct dips at 772, 846 and 938 nm in the reflection spectrum. These resonances are located within the photonic crystal bandgap of the bottom DBR, showing the role of the cavity effect in forming the specific resonances. Furthermore, almost the entire incident energy can be absorbed at each resonance, especially at the two longer wavelengths. The responsivity spectra of the MC-HE PD are shown in Fig. 6(d), which shows
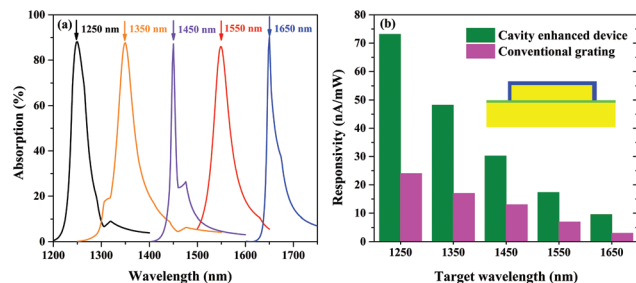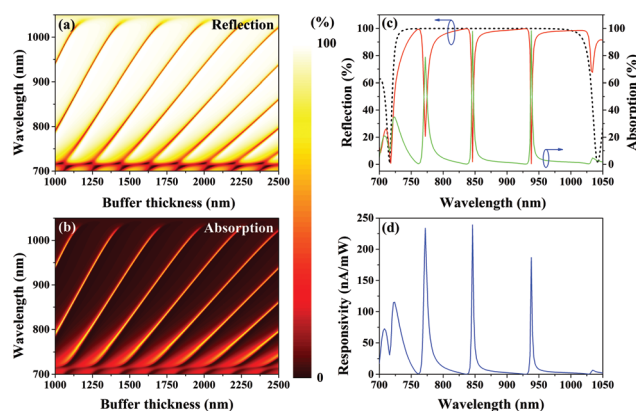

Fig. 5 (a) The absorption spectra for the 10 nm Ag layer for the operating wavelengths of 1250, 1350, 1450, 1550, and 1650 nm in the designed MC-HE PD; (b) the responsivities of the MC-HE PD and the conventional grating systems (the inset).

Fig. 6 The contour maps of the reflection (a) and the total absorption (b) as a function of the incident wavelength and buffer thickness in the MC-HE PD. (c) The reflection and absorption spectra of the MC-HE PD with a buffer thickness of 2000 nm, where the dashed line is the reflection spectrum of the bottom DBR. (d) The responsivity spectrum of the MC-HE PD for multiband hot-electron photodetection.
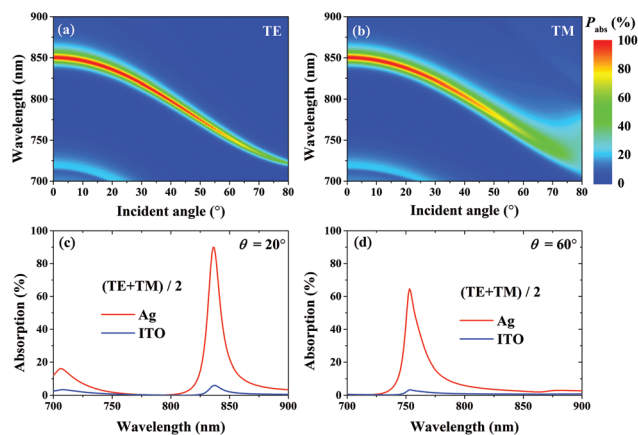
Fig. 7 The contour maps of total absorption as a function of the incident wavelength and angle for (a) TE and (b) TM incidences. The absorption spectra of Ag and ITO under unpolarized incidence for the angles of (c) 20° and (d) 60°.

device with 2-pairs of top DBR and a 193 nm buffer layer. For the absorption in Ag, finite-element simulations demonstrate a 21-fold enhancement in the microcavity-integrated device as compared to the absorption of 4.18% in the reference device. The examination of the spatial profile of the resistive losses reveals a highly asymmetrical generation of the hot electrons in the electrodes, leading to a strongly unidirectional photocurrent. Our electrical calculations further predict that the unbiased responsivity can be up to 239 nA mW^{-1}, which is more than an order of magnitude larger than that of the planar reference without a microcavity. In addition, at the infrared wavelength λ = 1550 nm, the responsivity can be ~2.5 times larger than that based on the conventional grating design. Further study indicates that perfect absorption can be maintained in the device with an ultrathin metal thickness, and multiband photodetection can be realized by modulating the cavity configuration.

Acknowledgements

that the responsivities at the three resonances can be comparable to that of the device with a resonance at λ = 850 nm.

Finally, we examine the performance of the MC-HE PD under oblique incidences, with which both the transverse electric (TE) and transverse magnetic (TM) incidences have to be considered. Fig. 7(a) and (b) show the contour maps of total absorption as a function of the incident wavelength and angle (θ) for TE and TM incidences, respectively. According to the Fabry–Perot (FP) cavity theory, the resonance wavelength will blueshift as the incident angle increases, which is consistent with the result in Fig. 7(a) and (b). The optical absorption efficiency is weakened gradually since less solar intensity (I) is incident into the device, based on Lambert's cosine law ($I \sim \cos\theta$). The unpolarized incidences calculated by taking the average of TE and TM incidences (*i.e.*, TE/2 + TM/2) under the incident angles of 20° and 60° are illustrated in Fig. 7(c) and (d), respectively. When θ = 20°, the peak absorption efficiency in Ag is slightly decreased to 90%, which is just slightly lower than that under normal incidence (92.4%). It is worth noting that the large absorption enhancement in the microcavity can be sustained over a wide range of incident angles, *e.g.*, at θ = 60°, P_{Ag} = 64.6%, showing a more than 14-fold absorption enhancement compared to the 4.18% result for the reference. As a result, the predicated photoresponsivity will show only a slight decrement under a wide range of incident angles.

4. Conclusion

We have presented the design of planar hot-electron photodetectors formed by integrating the TCO/semiconductor/metal structure into an asymmetric microcavity consisting of two DBRs and a buffer layer. It is found that the buffer layer thickness and the number of top DBR pairs determine the resonant wavelength and the absorption efficiency of the device, respectively. More than 98% of the incoming light is absorbed in the

References

1 M. W. Knight, H. Sobhani, P. Nordlander and N. J. Halas, *Science*, 2011, **332**, 702–704.

2 C. Scales and P. Berini, *IEEE J. Quantum Electron.*, 2010, **46**, 633–643.

3 K. Ueno and H. Misawa, *NPG Asia Mater.*, 2013, **5**, e61.

4 M. W. Knight, Y. Wang, A. S. Urban, A. Sobhani, B. Y. Zheng, P. Nordlander and N. J. Halas, *Nano Lett.*, 2013, **13**, 1687–1692.

5 A. Sobhani, M. W. Knight, Y. Wang, B. Zheng, N. S. King, L. V. Brown, Z. Fang, P. Nordlander and N. J. Halas, *Nat. Commun.*, 2013, **4**, 1643.

6 K.-T. Lin, H.-L. Chen, Y.-S. Lai and C.-C. Yu, *Nat. Commun.*, 2014, **5**, 3288.

7 W. Li and J. Valentine, *Nano Lett.*, 2014, **14**, 3510–3514.

8 I. Goykhman, B. Desiatov, J. Khurgin, J. Shappir and U. Levy, *Nano Lett.*, 2011, **11**, 2219–2224.

9 H. Chalabi, D. Schoen and M. L. Brongersma, *Nano Lett.*, 2014, **14**, 1374–1380.

10 K. Wu, Y. Zhan, C. Zhang, S. Wu and X. Li, *Sci. Rep.*, 2015, **5**, 14304.

11 T. Gong and J. N. Munday, *Nano Lett.*, 2015, **15**, 147–152.

12 K. Wu, Y. Zhan, S. Wu, J. Deng and X. Li, *J. Appl. Phys.*, 2015, **118**, 063101.

13 S. V. Boriskina, H. Ghasemi and G. Chen, *Mater. Today*, 2013, **16**, 375–386.

14 S. Ishii, S.-I. Inoue, R. Ueda and A. Otomo, *ACS Photonics*, 2014, **1**, 1089–1092.

15 M. L. Brongersma, N. J. Halas and P. Nordlander, *Nat. Nanotechnol.*, 2015, **10**, 25–34.

16 E. W. McFarland and J. Tang, *Nature*, 2003, **421**, 616–618.

17 C. Clavero, *Nat. Photonics*, 2014, **8**, 95–103.

18 J. Li, S. K. Cushing, P. Zheng, F. Meng, D. Chu and N. Wu, *Nat. Commun.*, 2013, **4**, 2651.

19 S. Mukherjee, F. Libisch, N. Large, O. Neumann, L. V. Brown, J. Cheng, J. B. Lassiter, E. A. Carter, P. Nordlander and N. J. Halas, *Nano Lett.*, 2013, **13**, 240–247.

20 P. J. Schuck, *Nat. Nanotechnol.*, 2013, **8**, 799–800.

21 A. Giugni, B. Torre, A. Toma, M. Francardi, M. Malerba, A. Alabastri, R. P. Zaccaria, M. I. Stockman and E. D. Fabrizio, *Nat. Nanotechnol.*, 2013, **8**, 845–852.

22 L. Novotny, *Phys. Rev. Lett.*, 2007, **98**, 266802.

23 Y. Zhan, K. Wu, C. Zhang, S. Wu and X. Li, *Opt. Lett.*, 2015, **40**, 4261–4264.

24 F. Wang and N. A. Melosh, *Nano Lett.*, 2011, **11**(12), 5426–5430.

25 K. Kishino, M. S. Ünlü, J.-I. Chyi, J. Reed, L. Arsenault and H. Morkoc, *IEEE J. Quantum Electron.*, 1991, **27**, 2025–2034.

26 M. S. Ünlü and S. Strite, *J. Appl. Phys.*, 1995, **78**, 607.

27 A. Ferreira, N. M. R. Peres, R. M. Ribeiro and T. Stauber, *Phys. Rev. B: Condens. Matter*, 2012, **85**, 115438.

28 J. R. Piper and S. Fan, *ACS Photonics*, 2014, **1**, 347–353.

29 A. Y. Polyakov, N. B. Smirnov, E. A. Kozhukhova, V. I. Vdovin, K. Ip, Y. W. Heo, D. P. Norton and S. J. Pearton, *Appl. Phys. Lett.*, 2003, **83**, 1575–1577.

30 H. Kim, H. Kim and D.-W. Kim, *J. Appl. Phys.*, 2010, **108**, 074514.

31 X. Wang, C. Liow, D. Qi, B. Zhu, W. R. Leow, H. Wang, C. Xue, X. Chen and S. Li, *Adv. Mater.*, 2014, **26**(21), 3506–3512.

32 X. Wang, C. Liow, A. Bisht, X. Liu, T. C. Sum, X. Chen and S. Li, *Adv. Mater.*, 2015, **27**(13), 2207–2214.

33 D. A. Kovacs, J. Winter, S. Meyer, A. Wucher and D. Diesing, *Phys. Rev. B: Condens. Matter*, 2007, **76**, 235408.

34 E. D. Palik, *Handbook of Optical Constants of Solids*, Academic, 1985.

35 Comsol Multiphysics, http://www.comsol.com/.

36 M. G. Moharam, E. B. Grann and D. A. Pommet, *J. Opt. Soc. Am. A*, 1995, **12**, 1068–1076.

37 X. Li, Y. Zhan and C. Wang, *Prog. Photovoltaics: Res. Appl.*, 2015, **23**, 628–636.

38 M. Furchi, A. Urich, A. Pospischil, G. Lilley, K. Unterrainer, H. Detz, P. Klang, A. M. Andrews, W. Schrenk, G. Strasser and T. Mueller, *Nano Lett.*, 2012, **12**, 2773–2777.

39 B. Y. Zheng, H. Zhao, A. Manjavacas, M. McClain, P. Nordlander and N. J. Halas, *Nat. Commun.*, 2015, **6**, 7797.

40 J. R. Bellingham, W. A. Phillips and C. J. Adkins, *J. Phys.: Condens. Matter*, 1990, **2**, 6207–6221.

41 M. P. Seah and W. A. Dench, *Surf. Interface Anal.*, 1979, **1**, 2–11.

42 Z. Yu, A. Raman and S. Fan, *Appl. Phys. A*, 2011, **105**, 329–339.

43 A. H. Gevorgyan and M. Z. Harutyunyan, *Phys. Rev. E: Stat. Phys., Plasmas, Fluids, Relat. Interdiscip. Top.*, 2007, **76**, 031701.

44 L. Qi, Z. Yang and T. Fu, *Phys. Plasmas*, 2012, **19**, 012509.

45 R. Zhao, T. Zhai, Z. Wang, Y. Wang and D. Liu, *Appl. Phys. B*, 2008, **93**, 853–857.